

# On the Formulation of Three-Dimensional Inverse Catenary for Embedded Mooring Line Modeling

M.A.L. Martins<sup>1</sup> and E.N. Lages<sup>1</sup>

**Abstract:** Embedded anchors have been widely used in offshore operations, and they are known to be effective and economical solutions to anchoring problems. Aiming at contributing to the definition and understanding of the embedded mooring line behavior, this paper expands the formulation adopted at DNV Recommended Practices, for two-dimensional modeling of the interaction between the seabed and the anchor line, to three-dimensional analysis. The formulation here presented, within an elegant differential geometry approach, can now model even out of plane lines. A reference problem is then defined and solved using the obtained governing equations. Corresponding equations are implemented and solved numerically in MATLAB<sup>®</sup> environment. Numerical results are also presented and discussed.

**Keywords:** Inverse catenary; Three-dimensional modeling; Embedded anchors.

## 1 Introduction

Finding and accessing offshore sources of oil and gas depends on the overall availability of the marine system. In such scenario, one fundamental and limiting aspect is the mooring system, which is crucial to maintain the floating unit position within limits. For such purpose, thrusters and mooring lines are used to withstand environmental loads due to wave, wind, and current. There are several types of mooring systems, and the applicability of each one depends on different aspects [Skop (1988); Colliat (2002); Chakrabarti (2005)].

A mooring line connects an anchor on the seafloor to a floating structure, and this system relies on the strength of the anchors, soil conditions, geometry and weight of the anchor, and size of anchor line. Those are some of the aspects that influence several parameters, such as penetration depth and anchor capacity.

---

<sup>1</sup> Scientific Computing and Visualization Laboratory, Technology Center, Federal University of Alagoas, Campus A. C. Simões - Av. Lourival de Melo Mota, s/n, Tabuleiro do Martins - Maceió/AL, Brazil. E-mail: {micheleagra, enl}@lccv.ufal.br

Embedded anchors are commonly used for the mooring of deepwater platforms as they are able to perfectly maintain the offset of floating facilities within design tolerances. As it penetrates the seabed, it uses soil resistance to hold the anchor in place, so that drilling and production operations can be carried out at a stable platform.

Embedded lines will cut through the seabed to some extent. The embedded part of the line generally forms an inverse catenary profile between the mudline and the pad-eye of the anchor. DNV Recommended Practices [Det Norske Veritas (2000, 2002)] describe the two-dimensional equations for modeling the interaction between the seabed and the embedded line in soil.

However, when the mooring system is in service, due to the influence of external loads, the mooring cable may produce a series of motions in a three-dimensional space. Thus, it is also important to analyze the out of plane behavior of the structure, to properly provide accurate analysis in order to predict its responses. The ability to properly understand and describe inverse catenary properties of the embedded line is fundamental to improve the mooring system performance.

Chi (2010) emphasizes the importance of considering the out of plane component by reporting that during the hurricanes Ivan, Katrina, and Rita in 2005, there were about seventeen offshore mobile drilling units drifting due to the failure of the mooring system. Partial failure of mooring systems for floating structure will subject drag anchor to loads having an appreciable component outside of the intended plane of loading. Therefore, under this circumstance, the anchor may travel out of the installation plane direction. Aubeny and Chi (2010) show that, if the self-weight of the anchor chain is neglected, the anchor chain configuration will lie always within a plane, although for general conditions of out-of-plane loading, the anchor chain will lie in an oblique plane defined by the direction of the anchor chain at the pad-eye and the mudline.

Aubeny, Gilbert, Randall, Zimmerman, McCarthy, Chen, Drake, Yeh, Chi, and Beemer (2011) conducted experimental investigations in order to increase understanding of embedment anchor behavior. They came into the conclusion that if the anchor line forms into a reverse catenary the anchor line and anchor trajectory will lie in an oblique plane. In such scenario, the tendency for the anchor to travel in a tilted plane will tend to reduce the ultimate embedment depth, and therefore ultimate capacity, of the anchor. Countering this effect is an observed increase in the anchor bearing factor, which will both cause the anchor to dive deeper and mobilize greater pullout capacity. Therefore, the ultimate pullout capacity under out-of-plane loading conditions could conceivably be greater than that under in-plane loading.

Thus, aiming at contributing to the definition and understanding of the embedded cable behavior, this paper expands the two-dimensional formulation presented by Vivatrat, Valent, and Ponterio (1982) and adopted at DNV Recommended Practices [Det Norske Veritas (2000, 2002)] to a three-dimensional analysis. The proposed formulation incorporates an elegant differential geometry approach, and can now model even out of plane lines.

## **2 Background**

Theoretical and experimental studies about two-dimensional inverse catenary modeling of embedded mooring lines were carried out in previous studies [Reese (1973); Gault and Cox (1974); Vivatrat, Valent, and Ponterio (1982); Degenkamp and Dutta (1989); Liu (2012)]. The prediction of the resultant anchor line load involves numerical integration of the governing differential equations, together with iteration of one of the unknown boundary conditions in order to match the known boundary conditions.

Vivatrat, Valent, and Ponterio (1982) assume a two-dimensional chain configuration. They developed the analytical model by assuming the embedded chain length as a summation of short line segments and expressing the equilibrium conditions of each segment. Such model follows the same principles as previous work done by Reese (1973) and Gault and Cox (1974) but makes no assumption about the shape of the embedded chain section. DNV Recommended Practices [Det Norske Veritas (2000, 2002)] used such formulation developed by Vivatrat, Valent, and Ponterio (1982) for planar line configuration.

Degenkamp and Dutta (1989) also present an analytical model of embedded chain under soil resistance, similar to the one presented by Vivatrat, Valent, and Ponterio (1982). They used a soil model to accurately predict the soil resistances to the chain inside soil and estimate critical design parameters, such as effective widths of the chain, based on laboratory tests.

In order to avoid the numerical solution by an incremental integration technique, as proposed by Degenkamp and Dutta (1989), Neubecker and Randolph (1995, 1996) suggested a simplified approach for the expressions of both the load development and chain profile. They developed an expression for the anchor chain tension and angle at the anchor pad-eye assuming the chain angle at the seabed is zero. The authors also considered that the self-weight of the chain has negligible effect on the chain profile and tension distribution when used in hard soils. However, in soft soils the chain weight may be significant with respect to the soil strength. In such case, to properly account for the self-weight of the chain, one has to assume that the chain is weightless and has to reduce the profile of normal resistance per unit

length by an amount equal to the chain weight per unit length.

Bang, Han, and Taylor (2001) describe the analytical solution for a portion of the mooring line on the seabed. The results of the field tests conducted in cohesive seafloor soils, and the resulting comparisons between the measured and calculated values are presented in detail.

To extend the inverse catenary equations to three-dimensional space, line tensions need to be described in three-dimensional vectors. Nie, Zimmerman, and Aubeny (2011) present an analysis of drag embedment anchor under out-of-plane loading. This analysis develops a set of three-dimensional inverse catenary equations based on the existing two-dimensional equations using two reference angles ( $\theta$  and  $\phi$ ) in spherical coordinates, one ( $\theta$ ) is measured from horizontal plane to the vector and is equivalent to the angle in 2D case, and the other ( $\phi$ ) is the angle of the projection on the horizontal plane.

Wang, Guo, and Yuan (2010) present a 3-D iterative procedure to solve the equilibrium equations of a set of deformed segments of the discretization of the embedded line according to new dip-down point tension defined after a pretensioning configuration. The geometric position of the deformed nodes is updated until the internal force of the upper segment is equal the prescribed external tension.

Liu, Liu, Zhao, and Wang (2013) propose an approach that enable the one to obtain not only the anchor behaviors such as the trajectory, penetration direction and ultimate embedment depth, but also the properties of the installation line for both the embedded and horizontal segments. In such study, the authors have derived the relationship between the tension and geometry of the embedded line, and the interactional equation between the anchor and embedded line based on the mechanical model for the embedded line. They introduced the concept of the initial embedment depth of the installation line (IEDL), and the reverse catenary equation and the equation for calculating the length of the embedded line were obtained for soils with a linear strength. The reverse catenary equation is then introduced into the kinematic model for drag anchors, which combines the drag anchor, the installation line and the movement of the anchor handling vessel (AHV) being an interactional system.

In a subsequent study, Liu, Liu, Zhao, and Wang (2014) used measured data to compare the predictions from reverse catenary equations applicable to sand previously developed by Liu, Liu, Zhao, and Wang (2013). The authors used specially developed measurement techniques (based on tilt transducers and photography) to investigate the reverse catenary profile of the embedded line, the effective length of the installation line, the relation between the vertical position and the drag angle at the shackle of the anchor, and the equivalent length of the installation line in a

model flume. By comparing with transient reverse catenary shapes of the embedded line during anchor penetration, the efficiency of the reverse catenary equations developed by Liu, Liu, Zhao, and Wang (2013) are well examined in sand through model flume tests.

Besides, Zhao and Liu (2013) present a large deformation finite element analysis using the Coupled Eulerian-Lagrangian (CEL) technique to investigate the tension and profile of embedded anchor line. In such study, parametric analysis are performed to evaluate the effects of the shear strength of clay, depth of attachment point, diameter of embedded anchor line, self weight of soil, self weight of anchor line, and frictional coefficient between the embedded anchor line and soil. By comparing with theoretical and numerical integration solutions, the authors demonstrate that the CEL technique is effective for simulating the anchor line-soil interactional problems.

This paper presents the three-dimensional analytical formulation for modeling the interaction between the seafloor and the embedded line. Such formulation allows the consideration of the soil tangential resistance, the effective weight of the line in soil, and the general case of line entering the soil at a specific angle. So, we consider that the seafloor reacts on the line with forces that are distributed along the length at the longitudinal and transverse directions, which are defined with respect to the directions of the Frenet trihedron [e.g., Lal and Arora (1989)]. With the obtained governing differential equations, it is defined a reference problem, where relevant equations are implemented and solved numerically in MATLAB<sup>®</sup> environment.

### 3 3-D inverse catenary

The three-dimensional static problem of an embedded anchor is considered, according to the scheme shown in Fig. 1. A coordinate system is defined with origin at the dip-down point, where the anchor line starts to embed, and with the  $z$ -axis normal to the seabed.

According to Fig. 1, the embedded line anchor in its static equilibrium configuration is defined by a total length  $L$  and projections  $H_x$  and  $H_y$  along the Cartesian  $x$  and  $y$  directions, respectively. Thus, the deepest end of the embedded line is connected to a perfectly fixed anchor on the seafloor at a depth  $P$ .

It is assumed that the line reacts internally with only axial forces, ignoring possible contributions of shear force, bending moment, and twisting moment. At the dip-down point acts a tension  $T_0$ , which orientation relative to the Cartesian system will be defined later. The seafloor reacts on the line with distributed forces along the length at the longitudinal and transverse directions, which are defined with respect to the directions of the Frenet trihedron [e.g., Lal and Arora (1989)]. The Frenet

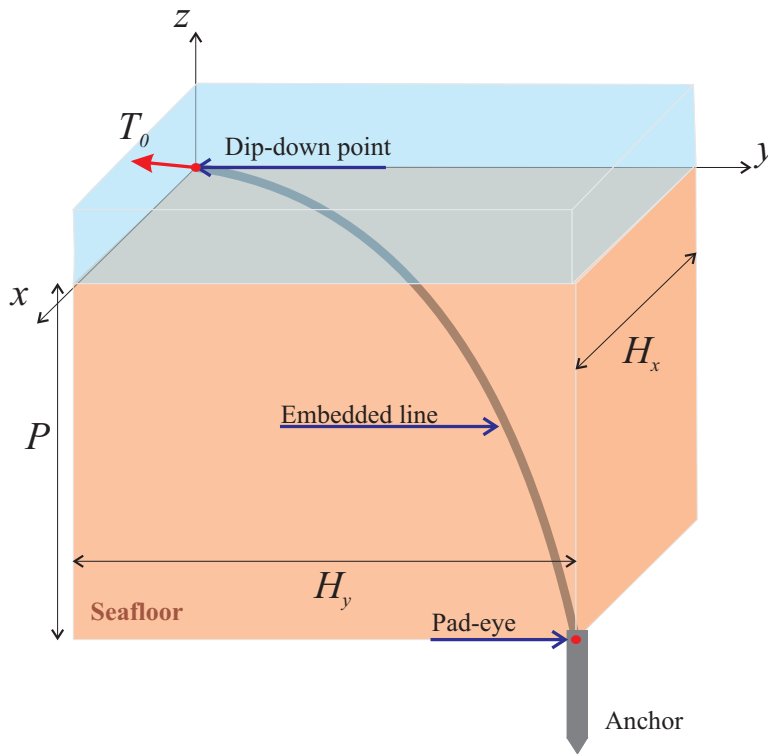


Figure 1: Diagram of three-dimensional line segment in soil.

trihedron establishes a local reference system to the geometry of the parametric curve, which is representative of the embedded line section.

Initially, we consider a parametric curve representing the embedded line as a function of the arc length  $s$ , measured from the dip-down point at the seabed. Isolating a small segment of length  $\Delta s$  of that embedded line, one can build up the free body diagram shown in Fig. 2, where  $\hat{\mathbf{t}}$ ,  $\hat{\mathbf{n}}$  and  $\hat{\mathbf{b}}$  represent, respectively, the orthonormal vectors of the Frenet trihedron in tangent, principal normal and binormal directions at the midpoint of the analyzed segment.

With respect to the forces in this diagram (Fig. 2),  $w$  is the weight of the embedded line per unit deformed length, which acts in the negative direction of the Cartesian  $z$ -axis,  $q_t$  is the soil reaction per unit length of the line along the tangent direction, acting in the dip direction of the line in the seabed, and  $q_n$  and  $q_b$  are the transverse components of the soil reaction per unit length of the line along the principal normal and binormal directions, respectively, acting in opposite directions to those.

Frenet-Serret formula [e.g., Lal and Arora (1989)] is used here to write the deriva-

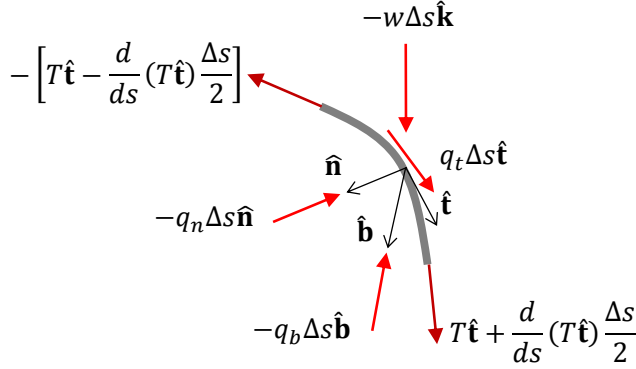


Figure 2: Free body diagram of a representative embedded line segment.

tive of the unit tangent vector at the midpoint of the segment, as follows:

$$\frac{d\hat{\mathbf{t}}}{ds} = \kappa \hat{\mathbf{n}} \tag{1}$$

where  $\kappa$  represents the circular curvature.

To use the same reference directions of all forces involved in this free body diagram (Fig. 2), one can rewrite the Cartesian unit vector  $\hat{\mathbf{k}}$  in relation to the unit vectors of the Frenet trihedron, as follows:

$$\hat{\mathbf{k}} = (\hat{\mathbf{k}} \cdot \hat{\mathbf{t}})\hat{\mathbf{t}} + (\hat{\mathbf{k}} \cdot \hat{\mathbf{n}})\hat{\mathbf{n}} + (\hat{\mathbf{k}} \cdot \hat{\mathbf{b}})\hat{\mathbf{b}} \tag{2}$$

where  $\cdot$  represents the dot product between the unit vectors. That leads to

$$\hat{\mathbf{k}} = t_z \hat{\mathbf{t}} + n_z \hat{\mathbf{n}} + b_z \hat{\mathbf{b}} \tag{3}$$

where  $t_z$ ,  $n_z$  and  $b_z$  are z-component of the unit vectors of the Frenet trihedron.

The balance of forces is imposed in accordance with the Maple [MAPLESOFT (2014)] code, as illustrated in Fig. 3.

According to the script shown in Fig. 3, we obtain the following equilibrium equations associated with the directions of the Frenet trihedron:

$$\frac{dT}{ds} = wt_z - q_t \tag{4}$$

$$\kappa = \frac{wn_z + q_n}{T} \tag{5}$$

```

> restart
Internal forces (axial only)
>  $Ti := -T \cdot \mathbf{t} + (dTds \cdot \mathbf{t} + T \cdot dt ds) \cdot \frac{\Delta s}{2} :$ 
>  $Tf := T \cdot \mathbf{t} + (dTds \cdot \mathbf{t} + T \cdot dt ds) \cdot \frac{\Delta s}{2} :$ 
External forces: self weight (negative z-direction) and longitudinal friction (opposite to the dip direction of the line), normal and binormal (contrary to the directions of the unit vectors of the Frenet trihedron associated with these directions)
>  $EF := -w \cdot \Delta s \cdot \mathbf{k} + qt \cdot \Delta s \cdot \mathbf{t} - qn \cdot \Delta s \cdot \mathbf{n} - qb \cdot \Delta s \cdot \mathbf{b} :$ 
Frenet-Serret formula
>  $dt ds := \kappa \cdot \mathbf{n} :$ 
Cartesian unit vector in the z-direction as a function of the unit vectors of the Frenet trihedron
>  $\mathbf{k} := tz \cdot \mathbf{t} + nz \cdot \mathbf{n} + bz \cdot \mathbf{b} :$ 
Balance of forces
>  $eqF := Ti + Tf + EF :$ 
>  $eqF := \text{simplify} \left( \frac{eqF}{\Delta s} \right) :$ 
Equilibrium equations
>  $\text{coeff}(eqF, \mathbf{t})$ 
 $dTds - w tz + qt$ 
>  $\text{coeff}(eqF, \mathbf{n})$ 
 $T\kappa - w nz - qn$ 
>  $\text{coeff}(eqF, \mathbf{b})$ 
 $-w bz - qb$ 

```

Figure 3: Maple code for determining the equilibrium equations.

$$q_b = -wb_z \tag{6}$$

Note that the particularization of such formulation for two-dimensional case lies in that presented by Vivatrat, Valent, and Ponterio (1982). In this case, considering a curve in the  $xz$ -plane, Eqs. (4), (5), and (6) can be particularized. Assuming  $\theta$  as the line inclination with  $x$ -axis,  $t_z$  turns to be  $-\sin \theta$  in Eq. (4),  $\kappa$  is  $\frac{d\theta}{ds}$  and  $n_z$  turns to be  $-\cos \theta$  in Eq. (5), and  $b_z$  is zero in Eq. (6), indicating that no soil reaction is mobilized in the binormal direction.

As  $w$  is the weight of the embedded line per unit deformed length, it is related to

$w_0$ , the weight per unit undeformed length, as

$$w = \frac{w_0}{1 + \frac{T}{EA_0}} \quad (7)$$

where  $EA_0$  is the axial rigidity of the line cross section, considering linear elastic behavior in strain engineering. As the correction factor of the weight of the embedded line per unit undeformed length ( $w_0$ ) to the weight of the embedded line per unit deformed length ( $w$ ) is approximately equal to 1 for typical values of tension and axial rigidity,  $w$  can be assumed equal to  $w_0$ , as considered by Vivatrat, Valent, and Ponterio (1982).

In addition to these equations, to assist in the explicit representation of the line geometry corresponding to the static equilibrium configuration, the spatial variation of the position vector  $\mathbf{r}$  for any point along the curve is described by the following differential equation:

$$\frac{d\mathbf{r}}{ds} = \hat{\mathbf{t}} \quad (8)$$

as the curve is being parameterized by the arc length [e.g., Lal and Arora (1989)]. In order to complete the line geometry description, other Frenet-Serret formula [e.g., Lal and Arora (1989)] is used here to write the binormal vector, as follows:

$$\frac{d\hat{\mathbf{b}}}{ds} = -\tau\hat{\mathbf{n}} \quad (9)$$

where  $\tau$  represents the torsion. The principal normal unit vector  $\hat{\mathbf{n}}$  can be determined at any point in the anchor line curve by applying the orthonormality condition with the two other unit vectors  $\hat{\mathbf{t}}$  and  $\hat{\mathbf{b}}$  of the Frenet trihedron.

About the soil reaction, several models for the interaction forces between the seabed and the embedded line, present in Eqs. (4), (5), and (6), can be tested and calibrated from experiments. However, extending the expressions presented in DNV Recommended Practices [Det Norske Veritas (2000, 2002)], these forces directly involved with tension  $T$ , as well as its spatial variation  $\frac{dT}{ds}$ , are assumed in the following formats:

$$q_t = \alpha_s s_u A_s \quad (10)$$

$$q_B = N_c s_u A_B \quad (11)$$

$$q_n = \sqrt{q_B^2 - q_b^2} \quad (12)$$

where  $q_B$  is the resultant soil force at transverse direction,  $\alpha$  is the adhesion factor,  $s_u$  is the undrained shear strength,  $N_c$  is the bearing capacity factor,  $A_S$  is the effective surface area and  $A_B$  is the effective bearing area, both per unit length of the line.

Reference values for these parameters are suggested in DNV Recommended Practices [Det Norske Veritas (2000, 2002)] and presented in Tab. 1, depending on line type and line effective diameter ( $d$ ). Such values were defined based on the back-fitting analysis reported by Eklund and Strøm (1998), and are recommended for the embedded part of the anchor line in clay. For the undrained shear strength, the DNV Recommended Practices [Det Norske Veritas (2000, 2002)] suggest the use of direct simple shear strength  $s_{uD}$ .

Table 1: Reference values for adhesion factor ( $\alpha$ ), bearing capacity factor ( $N_c$ ), effective surface area ( $A_S$ ) and effective bearing area ( $A_B$ ) for wire and chain.

Line type	$\alpha$	$N_c$	$A_S$	$A_B$
Chain	0.4 to 0.6	9 to 14	$11.3 d$	$2.5 d$
Wire	0.2 to 0.4	9 to 14	$\pi d$	$d$

According to this perfectly rigid-plastic model, variations in the magnitudes of these distributed forces can be incorporated due to spatial variations of its parameters, especially along the depth.

#### 4 Reference problem

As a reference problem, we assume that the tension ( $T_0$ ) and the orientation of the Frenet trihedron at the upper end of the embedded line are known, as well as the penetration depth ( $P$ ) and all information regarding the soil resistance. Thus, it is possible to obtain the parametric curve ( $\mathbf{r}$ ), its total length ( $L$ ) and horizontal projections ( $H_x$  and  $H_y$ ) of the embedded line after proper analysis of the governing equations.

Taking the depth of anchorage  $P$  as a problem input (which is more natural to prescribe, instead of its total length  $L$ ), it is convenient to write the governing differential equations as a function of a new independent variable  $p$ , measured vertically downward from the seabed. Thus, there is a relationship between the infinitesimal terms  $ds$  and  $dp$ , as follows:

$$ds = -\frac{1}{t_z} dp \quad (13)$$

where  $t_z$  is the  $z$ -component of the unit tangent vector.

Then, the boundary value problem [e.g., Kreyszig (2011)] to be solved is the system of first order differential equations given by

$$\frac{dT}{dp} = -w + \frac{q_t}{t_z} \quad (14)$$

$$\frac{ds}{dp} = -\frac{1}{t_z} \quad (15)$$

$$\frac{d\mathbf{r}}{dp} = -\frac{1}{t_z} \hat{\mathbf{t}} \quad (16)$$

$$\frac{d\hat{\mathbf{t}}}{dp} = -\frac{\kappa}{t_z} \hat{\mathbf{n}} \quad (17)$$

$$\frac{d\hat{\mathbf{b}}}{dp} = \frac{\tau}{t_z} \hat{\mathbf{n}} \quad (18)$$

where the circular curvature  $\kappa$  is calculated using Eq. (5), the torsion  $\tau$  is prescribed as a non-negative function of the current depth  $p$ , and the unit vector  $\hat{\mathbf{n}}$  is determined by applying the orthonormality condition with  $\hat{\mathbf{t}}$  and  $\hat{\mathbf{b}}$ . In order to have a practical meaning of the curvature and torsion, considering an helix with ratio  $R$  and step  $S$ , these geometric indicators are equal to  $\frac{R}{R^2+(\frac{S}{2\pi})^2}$  and  $\frac{\frac{S}{2\pi}}{R^2+(\frac{S}{2\pi})^2}$ , respectively.

In this case, the embedded segment of the mooring line can take any shape, including out of plane line. We highlight that Nie, Zimmerman, and Aubeny (2011) also present a three-dimensional approach for the analysis of embedded mooring line. However, they develop the formulation based on projection angles in spherical coordinates, limiting the analysis to lines in vertical plane.

Equations (14) to (18) are subject to the following boundary conditions, taking the independent variable  $p$  equal to zero, i.e., at the dip-down point on the seabed:

$$T(0) = T_0 \quad (19)$$

$$s(0) = 0 \quad (20)$$

$$\mathbf{r}(0) = \mathbf{0} \quad (21)$$

$$\hat{\mathbf{t}}(0) = \hat{\mathbf{t}}_0 \quad (22)$$

$$\hat{\mathbf{b}}(0) = \hat{\mathbf{b}}_0 \quad (23)$$

Such reference problem is implemented in MATLAB<sup>®</sup> [MATHWORKS (2014)], in which the mathematical function *ode45* [Shampine and Reichelt (1997)] is used to

numerically integrate the system of first order differential equations. This function *ode45* is an explicit Runge-Kutta code based on the Dormand-Prince (4,5) pair [Dormand and Prince (1980)].

Figure 4 shows the implemented code of the auxiliary function that describes this problem, which is called by the numerical integration function *ode45*. This general code supports any soil reaction model that is described by parameter *soil*.

```
function dfdp=invcat3dode(p,f,~,EA0,w0,soil,ftau)
% -----
% Auxiliary function for the integration of the governing SODE of the
% 3D problem of inverse catenary.
% -----
% Parameters:
% p      (I) - Depth of current cross section.
% f      (I) - Integrated functions values (tension, arc length, position
%            vector, unit tangent vector, and binormal vector).
% EA0    (I) - Axial rigidity of the cross section.
% w0     (I) - Weight per unit length of the unstrained embedded line.
% soil   (I) - Structure comprising the name and parameters of the
%            function of the soil reaction in tangent and transverse
%            directions.
% ftau   (I) - Torsion function name.
% dfdp   (O) - Derivatives of the integrated functions.
% -----

% Tension at current section
T=f(1,1);

% Weight per unit length of the strained embedded line
w=w0/(1+T/EA0);

% Unit tangent, binormal, and principal normal vector
t=f(6:8,1);
b=f(9:11,1);
n=cross(b,t);

% Distributed soil forces calculus at binormal, tangent, transverse,
% and principal normal directions, as a function of the current depth
qb=-w*b(3);
[qt,qT]=feval(soil.fn,p,soil.par);
qn=sqrt(qT^2-qb^2);

% Circular curvature and torsion
k=(w*n(3)+qn)/T;
tau=feval(ftau,p);

% Derivatives of the integrated variables (tension, arc length,
% position vector, unit tangent vector, and binormal vector)
dfdp(1,1)=-w+qt/t(3);
dfdp(2,1)=-1/t(3);
dfdp(3:5,1)=-t/t(3);
dfdp(6:8,1)=-k*n/t(3);
dfdp(9:11,1)=tau*n/t(3);
```

Figure 4: MATLAB® code for the integration of the governing system of ordinary differential equations.

## 5 Numerical example

As an illustrative example of the implemented application, we consider a mooring line presented by Wang, Guo, and Yuan (2010). In such example, the interaction between an anchor chain and the seabed is considered, with penetration depth ( $P$ ) equal to 20.0m. The effective weight of unstrained chain in soil per unit length ( $w_0$ ) is 2.52kN/m, and the nominal chain diameter ( $d$ ) is 0.127m, with axial rigidity of the line cross section ( $EA_0$ ) equal to 1199.7MN. The effective bearing area ( $A_B$ ) is 2.5  $d$  (Tab. 1), but the effective surface area ( $A_S$ ) is considered equal to 8.0  $d$ . The adhesion factor of the chain in soil ( $\alpha$ ) is assumed as 1.0, in order to reproduce the same soil reaction force in tangent direction described by Wang, Guo, and Yuan (2010). The soil provides an undrained shear strength ( $s_u$ ) of 6kPa in a depth of 3.0m from which it grows at a rate of 1.26kPa/m. Finally, according to Degenkamp and Dutta (1989), the bearing-capacity factor ( $N_c$ ) increases from 5.14 to 7.6 from the seabed surface to a depth of 6 times the nominal chain diameter, from which it remains constant in value.

It is important to notice that the example presented in this section does not meet the condition that the ratio between the normal and tangential resistances is constant over the depth, as assumed in the analytical formulations presented by Neubecker and Randolph (1995) and Liu, Liu, Zhao, and Wang (2013).

Figure 5 shows the implemented code of the auxiliary function that describes the reaction forces of this soil, which is called during the integration of the governing system of ordinary differential equations.

To help at the definition of the unit vectors  $\hat{\mathbf{t}}_0$  and  $\hat{\mathbf{b}}_0$  present in boundary conditions given by Eqs. (22), and (23), respectively, three auxiliary angles  $\alpha_0$ ,  $\beta_0$ , and  $\gamma_0$  are considered in the sequence shown in Fig. 6, from left to right.

According to Fig. 6, at first the Frenet trihedron is oriented according to the Cartesian directions. Then, with angle  $\alpha_0$ , the trihedron is initially rotated around the Cartesian  $z$ -axis. Later, with angle  $\beta_0$ , the trihedron is rotated around the current principal normal unit vector. Finally, with angle  $\gamma_0$ , the trihedron is rotated around the current tangent unit vector.

Regarding the computational effort demanded to solve the proposed formulation, it takes less than 5 hundredths of a second to run each of the following cases. Such cases were run in a machine with the following characteristics: Windows 7 64-bits, MATLAB® R2011a, Intel® Core™ i7-2620M CPU @ 2.70 GHz 2.70 GHz, and 8GB RAM.

```

function [qt,qT]=cmes_ex_soil(p,par)
% -----
% Soil reaction function.
% -----
% Parameters:
% p (I) - Current depth (m).
% par (I) - Structure with nominal chain diameter (m).
% qt (O) - Soil reaction in tangent direction (kN/m).
% qT (O) - Soil reaction in transverse direction (kN/m).
% -----

% Nominal chain diameter (m)
d=par.d;

% Effective surface and bearing areas per unit length of the line (m^2/m)
As=8*d;
Ab=2.5*d;

% Adhesion factor
alpha=1.0;

% Bearing capacity factor
if p>6*d
    Nc=7.6;
else
    Nc=5.14+(7.6-5.14)/(6*d)*p;
end

% Undrained shear strength of the soil (kPa)
if p<=3
    su=6;
else
    su=6+1.26*(p-3);
end

% Soil reaction in tangent and transverse directions (kN/m)
qt=alpha*su*As;
qT=Nc*su*Ab;
    
```

Figure 5: MATLAB® code for soil reaction forces.

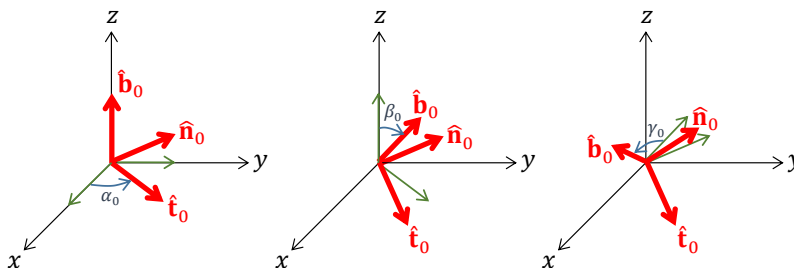


Figure 6: Auxiliary angles for the definition of Frenet trihedron at the top of the line.

### 5.1 Vertical plane line

Initially, to validate the three-dimensional formulation presented in this work, we consider two pretension processes presented by Wang, Guo, and Yuan (2010), with vertical plane lines.

In the first pretension process, a tension on the upper end of the embedded line gradually increases from 2000 kN to 4000 kN, and keeps inclination of  $45^\circ$  with Cartesian  $x$ -axis. Figure 7 shows the implemented MATLAB<sup>®</sup> code of the function used to run this simulation. Table 2 summarizes the main numerical results obtained in this first pretension process.

Table 2: Summary of the results for the tension level variation of the first pretension process.

<b>Tension level (kN)</b>	<b>Line length (m)</b>	<b>Horizontal projection (m)</b>	<b>Anchor tension (kN)</b>	<b>Anchor inclination</b>
2000	24.9	14.5	1583	71.86°
2400	25.3	15.3	1975	67.37°
2800	25.6	15.8	2369	64.20°
3200	25.9	16.3	2764	61.83°
3600	26.1	16.7	3160	59.99°
4000	26.3	16.9	3557	58.52°

According to the obtained results (Tab. 2), as one increases the tension level, the line requires a greater length ( $L$ ) and, consequently, larger horizontal projection ( $H_x$ ). In addition, the tension at the anchor increases, while anchor inclination reduces. All numerical results summarized in Tab. 2 are in perfectly agreement with the results presented by Wang, Guo, and Yuan (2010).

In the second pretension process, a tension on the upper end of the embedded line keeps 2000 kN, and the inclination gradually decreases from  $45.00^\circ$  to  $33.75^\circ$  with respect to the Cartesian  $x$ -axis. Table 3 summarizes the main numerical results obtained in this second pretension process.

According to the obtained results (Tab. 3), as one decreases the top angle inclination, the line requires a greater length ( $L$ ) and, consequently, larger horizontal projection ( $H_x$ ). In addition, the tension at the anchor decreases, while anchor inclination reduces. Once again, all numerical results summarized in Tab. 3 are in perfectly agreement with the results presented by Wang, Guo, and Yuan (2010) for this second pretension process.

```

function cmes_ex_pp1
% -----
% CMES example: pretension process with increasing of tension.
% -----

% Auxiliary angles for the definition of the unit vectors t0 and b0 (rad)
alpha0=0*pi/180;
beta0=135*pi/180;
gamma0=90*pi/180;

% Tension at the dip-down point (kN)
T0=2000:400:4000;

% Penetration depth (m)
P=20;

% Axial rigidity of the cross section (kN)
EA0=1199700;

% Weight per unit length of the unstrained embedded line (kN/m)
w0=2.52;

% Nominal chain diameter (m)
d=0.127;

% Soil structure comprising the name and parameters of the function
% of the soil reaction in tangent and transverse directions
soil.fn='cmes_ex_soil';
soil.par.d=d;

% Unit vectors t0 and b0
t0=[cos(beta0)*cos(alpha0) cos(beta0)*sin(alpha0) -sin(beta0)];
b0=[sin(beta0)*cos(alpha0) sin(beta0)*sin(alpha0) cos(beta0)];
b0=b0+cross(t0,b0)*sin(gamma0)+cross(t0,cross(t0,b0))*(1-cos(gamma0));

% Analyses and results
disp(' -----');
disp(' | T0 | L | Hx | Ta | Anga | ');
disp(' | (kN) | (m) | (m) | (kN) | (o) | ');
disp(' -----');

for i=1:length(T0),

    % Integration of the governing SODE
    [~,f]=ode45('invcat3dode',[0 P],[T0(i) 0 0 0 0 t0 b0], ...
        [],EA0,w0,soil,@(p)0);

    % Summary
    disp([' | ' num2str(T0(i)) ' ...
        | ' num2str(f(end,2),'%.1f') ' ...
        | ' num2str(-min(f(:,3)),'%.1f') ' ...
        | ' num2str(f(end,1),'%.0f') ' ...
        | ' num2str(acos(-f(end,6))*180/pi,'%.2f') ' | ']);

end

disp(' -----');

```

Figure 7: MATLAB® code for the first pretension process.

Table 3: Summary of the results for the inclination variation of the second pretension process.

<b>Inclination</b>	<b>Line length (m)</b>	<b>Horizontal projection (m)</b>	<b>Anchor tension (kN)</b>	<b>Anchor inclination</b>
45.00°	24.9	14.5	1583	71.86°
42.75°	25.6	15.6	1574	70.24°
40.50°	26.4	16.8	1565	68.69°
38.25°	27.2	18.0	1555	67.21°
36.00°	28.1	19.4	1544	65.80°
33.75°	29.1	20.7	1532	64.47°

## 5.2 Inclined plane line

In a next step, it is assumed as reference problem the case of a horizontal tension of 2000 kN at the upper end of the embedded line. It is intended to analyze the influence of working with embedded lines corresponding to planar curves contained in planes with inclinations to the Cartesian  $xz$ -plane. The angles  $\alpha_0$  and  $\beta_0$  are set to be  $0^\circ$  and  $180^\circ$ , respectively, and  $\gamma_0$  varies, assuming values of  $21^\circ$ ,  $34.56^\circ$ ,  $60^\circ$ , and  $90^\circ$ . The later value to  $\gamma_0$  corresponds to a vertical plane line.

Respectively, Figs. 8 and 9 show the three-dimensional static configurations of the embedded line and the tension variation along the arc length of the line for the four analyzed cases.

In Fig. 8 the Cartesian coordinates are measured from the anchor, and auxiliary plane shades are used to better visualize these four plane lines. When the inclination angle  $\gamma_0$  is equal to  $34.56^\circ$ , the tangent to the mooring line is perpendicular to the Cartesian  $x$ -axis at the pad-eye. When the inclination angle  $\gamma_0$  is smaller than this value, as  $21^\circ$ , the geometry of the line describes a reverse curve in  $xy$ -plane and  $xz$ -plane, i.e., a non-monotonic curve in Cartesian  $x$ -axis.

Figure 9 shows that the resulting tension relief is equivalent for the four analyzed cases during the first 40 m of the arc length from the dip-down point.

Table 4 summarizes the main numerical results obtained in this analysis. According to the obtained results (Tab. 4), as one increases the inclination of the plane which contains the embedded line curve, with respect to the Cartesian  $z$ -axis, the line requires a greater length ( $L$ ) and, consequently, larger horizontal projections ( $H_x$  and  $H_y$ ). In addition, from the upper end of the embedded line to the anchor, there is a tension relief at the anchor corresponding to 59.3%, 56.8%, 47.4%, and 26.7%

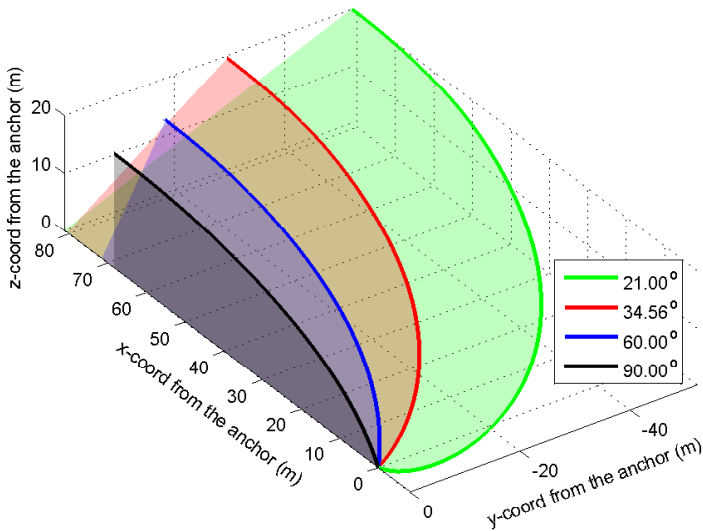


Figure 8: Three-dimensional static configurations for the variation of the plane inclination.

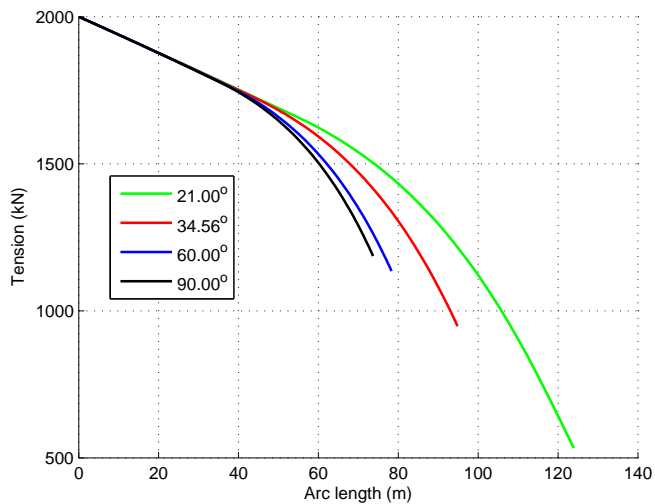


Figure 9: Tension variation along the length of the three-dimensional embedded line for the variation of the plane inclination.

of the force applied at the dip-down point.

Table 4: Numerical results for the variation of the plane inclination.

<b>Inclination</b> $\gamma_0$	<b>Line</b> <b>length</b> <b>(m)</b>	<b>Horizontal</b> <b>projection</b> $H_x$ (m)	<b>Horizontal</b> <b>projection</b> $H_y$ (m)	<b>Anchor</b> <b>tension</b> <b>(kN)</b>
21.00°	123.9	89.6	52.1	533
34.56°	94.9	80.6	29.0	948
60.00°	78.3	71.6	11.5	1135
90.00°	73.7	68.4	0.0	1186

### 5.3 Out of plane line

Now, the case of a horizontal tension of 2000kN at the upper end of the embedded line is assumed again, but now, it is intended to analyze the influence of working with embedded lines corresponding to out of plane lines. The angles  $\alpha_0$ ,  $\beta_0$ , and  $\gamma_0$  are set to be  $0^\circ$ ,  $180^\circ$ , and  $90^\circ$ , respectively, and torsion ( $\tau$ ) is constant along the mooring line, assuming values of 0.000, 0.006, 0.012, and 0.018. Note that torsion ( $\tau$ ) equal to 0.000 corresponds to a vertical plane line.

Respectively, Figs. 10 and 11 show the three-dimensional static configurations of the embedded line and the tension variation along the arc length of the line for the four analyzed cases.

In Fig. 10 the Cartesian coordinates are measured from the anchor, and auxiliary shades are used to better visualize these plane and out of plane lines.

Figure 11 shows that tension relief is equivalent during the first 50m of the arc length from the dip-down point.

Table 5 summarizes the main numerical results obtained in this analysis. According to the obtained results (Tab. 5), as one increases the torsion of the embedded line curve, the line requires a greater length ( $L$ ) and, consequently, larger horizontal projections ( $H_x$  and  $H_y$ ). In addition, from the upper end of the embedded line to the anchor, there is a tension relief at the anchor corresponding to 59.3%, 58.7%, 56.0% and 44.5% of the force applied at the dip-down point.

Finally, we will analyze the influence of torsion variation along the mooring line. We assume a reference value of torsion equal to 0.018, but considering constant torsion, quadratic reduction to zero, and linear reduction to zero of the torsion with the depth from the dip-down point to the pad-eye.

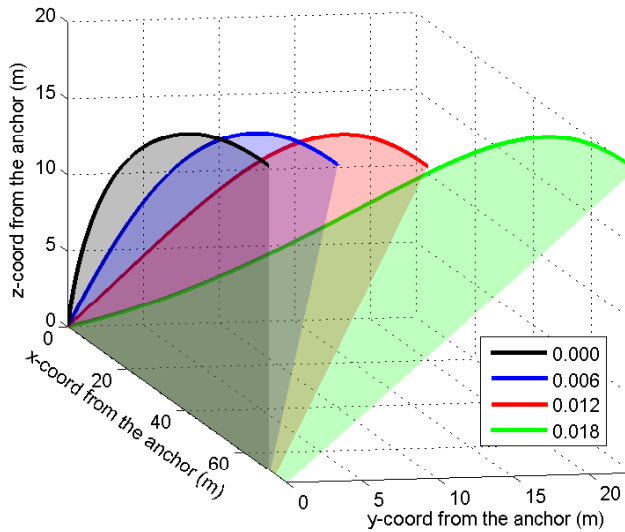


Figure 10: Three-dimensional static configurations for mooring lines with constant torsion.

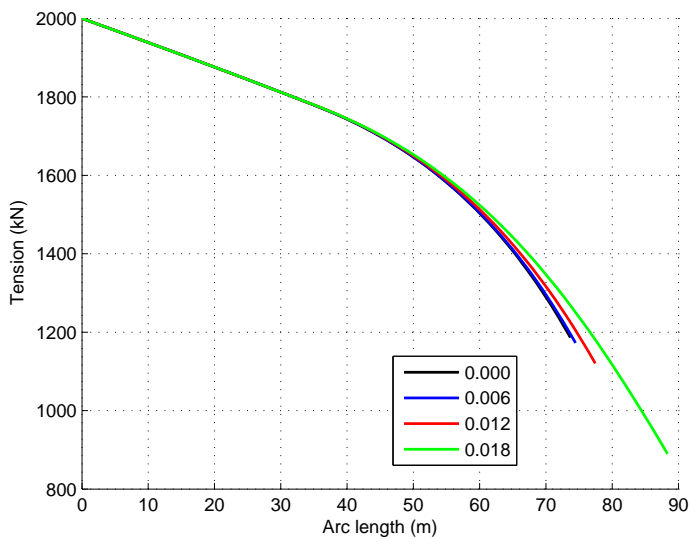


Figure 11: Tension variation along the length of the three-dimensional embedded lines with constant torsion.

Table 5: Numerical results for mooring lines with constant torsion.

Torsion $\tau$	Line length (m)	Horizontal projection $H_x$ (m)	Horizontal projection $H_y$ (m)	Anchor tension (kN)
0.000	73.7	68.4	0.0	1186
0.006	74.5	68.9	4.5	1173
0.012	77.5	70.7	10.1	1120
0.018	88.4	74.6	23.0	890

Respectively, Figs. 12 and 13 show the three-dimensional static configurations of the embedded line and the tension variation along the arc length of the line for the three analyzed cases.

In Fig. 12 the Cartesian coordinates are measured from the anchor, and auxiliary shades are used to better visualize these out of plane lines.

Figure 13 shows that tension relief is almost equivalent along the arc length of the mooring lines from the dip-down point.

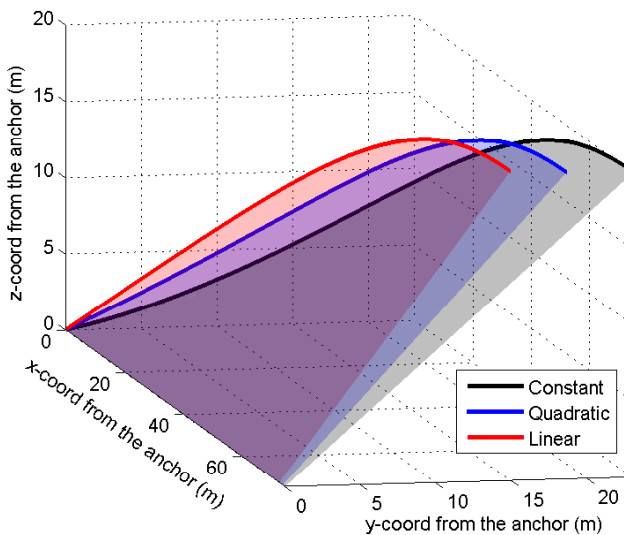


Figure 12: Three-dimensional static configurations for mooring lines with constant and variable torsion.

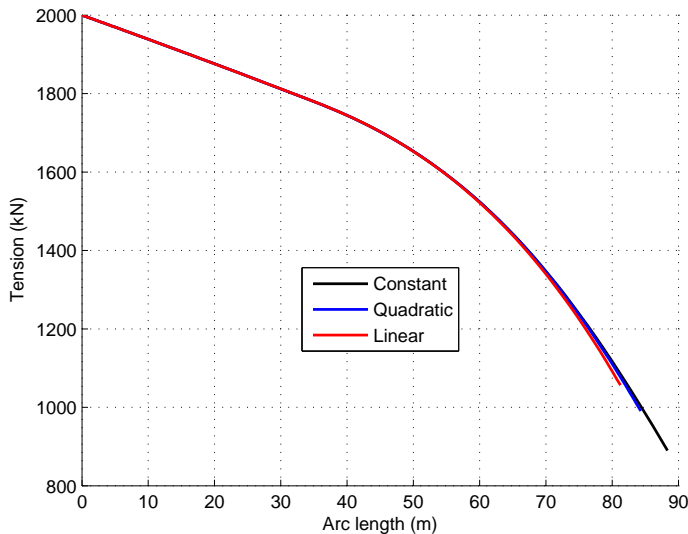


Figure 13: Tension variation along the length of the three-dimensional embedded lines with constant and variable torsion.

Table 6 summarizes the main numerical results obtained in this analysis. According to the obtained results (Tab. 6), as more twisted is the embedded line curve, the line requires a greater length ( $L$ ) and, consequently, larger horizontal projections ( $H_x$  and  $H_y$ ). In addition, from the upper end of the embedded line to the anchor, there is a tension relief at the anchor corresponding to 44.5%, 49.6%, and 52.8% of the force applied at the dip-down point.

Table 6: Numerical results for mooring lines with constant and variable torsion.

<b>Torsion</b> $\tau$	<b>Line</b> <b>length</b> (m)	<b>Horizontal</b> <b>projection</b> $H_x$ (m)	<b>Horizontal</b> <b>projection</b> $H_y$ (m)	<b>Anchor</b> <b>tension</b> (kN)
Constant	88.4	74.6	23.0	890
Quadratic	84.3	73.8	18.8	991
Linear	81.2	72.7	15.3	1056

## 6 Concluding remarks

The two-dimensional formulation of the interaction between the embedded line and the soil, presented by Vivatrat, Valent, and Ponterio (1982) and adopted at DNV Recommended Practices [Det Norske Veritas (2000, 2002)], was extended and verified for three-dimensional static analysis.

Within an elegant differential geometry approach, we can now model vertical plane, inclined plane, and even out of plane lines. This can be done by controlling the boundary conditions of the unit vectors  $\hat{\mathbf{t}}_0$  and  $\hat{\mathbf{b}}_0$  at the dip-down point, as well as torsion  $\tau$  along the embedded line.

Our proposed formulation considers the weight of the embedded line per unit deformed length ( $w$ ) physically consistent with the weight of the embedded line per unit undeformed length ( $w_0$ ) of the line, even though those values are very close when considering typical situations of the axial tension and rigidity, as in Vivatrat, Valent, and Ponterio (1982). This correction factor does not result in any significant computational overhead to the process of integration of the governing equations, and we kept this factor in our computer code (Fig. 4).

This soil-line interaction model considers the reaction of the seabed on the embedded line assuming its maximum resistance, which may vary with the depth of the analyzed point. Thus, that characterizes a load capacity problem, i.e., for a tension prescribed at the dip-down point, the line geometry seeks for its static equilibrium requiring the soil maximum resistance.

In the case of a tension relief at the dip-down point, as occurs in a dynamic time domain analysis [e.g., Silveira, Lages, and Ferreira (2012)], this model needs to be modified because it does not consider the unloading phase of the soil behavior. Thus, a tension relief at the dip-down point, determines a new geometry of the line, keeping the soil reaction at its resistance limit, which is not physically consistent.

This article presents results which were obtained following the reproducible research guidelines [e.g., Vandewalle, Kovacevic, and Vetterli (2009)]. All the relevant information is available at <http://loi.lccv.ufal.br/art-invcat3d>.

**Acknowledgement:** The second author acknowledges fellowship provided by the Brazilian Federal Council CNPq.

## References

**Aubeny, C. P.; Chi, C.-M.** (2010): Trajectory prediction for drag embedment anchors under out of plane loading. In Susan, G.; White, D.(Eds): *Proceedings of*

*the 2nd International Symposium on Frontiers in Offshore Geotechnics*, pp. 699–703, Perth, Australia.

**Aubeny, C. P.; Gilbert, R.; Randall, R.; Zimmerman, E. H.; McCarthy, K.; Chen, C.-H.; Drake, A.; Yeh, P.; Chi, C.-M.; Beemer, R.** (2011): The performance of drag embedment anchors (dea). Technical report, Offshore Technology Research Center, Texas A&M University, 2011.

**Bang, S.; Han, H.; Taylor, R. J.** (2001): Development and validation of mooring line analysis in cohesive seafloor. *International Journal of Offshore and Polar Engineering*, vol. 11, no. 2, pp. 141–146.

**Chakrabarti, S. K.** (2005): *Handbook of offshore engineering*, volume 2. Elsevier, 1 edition.

**Chi, C.-M.** (2010): *Plastic limit analysis of offshore of offshore foundation and anchor*. PhD thesis, Texas A&M University, August, 2010.

**Colliat, J. L.** (2002): Anchors for Deepwater to Ultradeepwater Moorings. In *Proceedings of the 34th Annual Offshore Technology Conference*, Houston, USA.

**Degenkamp, G.; Dutta, A.** (1989): Soil resistances to embedded anchor chain in soft clay. *Journal of Geotechnical Engineering-ASCE*, vol. 115, no. 10, pp. 1420–1438.

**Det Norske Veritas** (2000): Recommended Practice RP-E301: Design and installation of fluke anchors in clay, 2000.

**Det Norske Veritas** (2002): Recommended Practice RP-E302: Design and installation of plate anchors in clay, 2002.

**Dormand, J. R.; Prince, P. J.** (1980): A Family of Embedded Runge-Kutta Formulae. *Journal of Computational and Applied Mathematics*, vol. 6, no. 1, pp. 19–26.

**Eklund, T.; Strøm, P.** (1998): Back-fitting Analysis of Fluke Anchor Tests in Clay, DNV Report No. 96-3385, Rev. 03, dated 16 September 1997. Technical report, Det Norske Veritas, Hovik, 1998.

**Gault, J. A.; Cox, W. R.** (1974): Method for predicting geometry and load distribution in an anchor chain from a single point mooring buoy to a buried anchorage. In *Proceedings of the 6th Annual Offshore Technology Conference*, Houston, USA.

**Kreyszig, E.** (2011): *Advanced Engineering Mathematics*. John Wiley & Sons, 10 edition.

**Lal, B.; Arora, S.** (1989): *Three dimensional differential geometry*. Atma Ram & Sons, 5 edition.

- Liu, H.** (2012): Recent study of drag embedment plate anchors in China. *Journal of Marine Science and Application*, vol. 11, no. 4, pp. 393–401.
- Liu, H.; Liu, C.; Zhao, Y.; Wang, C.** (2013): Reverse catenary equation of the embedded installation line and application to the kinematic model for drag anchors. *Applied Ocean Research*, vol. 43, pp. 80–87.
- Liu, H.; Liu, C.; Zhao, Y.; Wang, C.** (2014): Comparative study of reverse catenary properties of the installation line for drag anchors. *Applied Ocean Research*, vol. 48, pp. 42–54.
- MAPLESOFT** (2014): *Maple 16*, 2014.
- MATHWORKS** (2014): *MATLAB*, 2014.
- Neubecker, S. R.; Randolph, M. F.** (1995): Profile and frictional capacity of embedded anchor chains. *Journal of Geotechnical Engineering*, vol. 121, no. 11, pp. 797–803.
- Neubecker, S. R.; Randolph, M. F.** (1996): The performance of drag anchor and chain systems in cohesive soil. *Marine Georesources & Geotechnology*, vol. 14, no. 2, pp. 77–96.
- Nie, C.; Zimmerman, E. H.; Aubeny, C. P.** (2011): Three-dimensional analysis of drag embedment anchor mooring systems under out of plane loads. In *Oceans 2011*. MTS/IEEE OCEANS Conference, Kona, HI, SEP 19-22, 2011.
- Reese, L. C.** (1973): A design method for an anchor pile in a mooring system. In *Proceedings of the 5th Annual Offshore Technology Conference*, Houston, USA.
- Shampine, L. F.; Reichelt, M. W.** (1997): The MATLAB ODE Suite. *SIAM Journal on Scientific Computing*, vol. 18, no. 1, pp. 1–22.
- Silveira, E. S. S.; Lages, E. N.; Ferreira, F. M. G.** (2012): DOOLINES: an object-oriented framework for non-linear static and dynamic analyses of offshore lines. *Engineering with Computers*, vol. 28, no. 2, pp. 149–159.
- Skop, R. A.** (1988): Mooring systems: a state-of-the-art review. *Journal of Offshore Mechanics and Arctic Engineering*, vol. 110, pp. 365–372.
- Vandewalle, P.; Kovacevic, J.; Vetterli, M.** (2009): Reproducible research in signal processing. *IEEE Signal Processing Magazine*, vol. 26, no. 3, pp. 37–47.
- Vivatrat, V.; Valent, P. J.; Ponterio, A. A.** (1982): The influence of chain friction on anchor pile design. In *Proceedings of the 14th Annual Offshore Technology Conference*, Houston, USA.
- Wang, L.-Z.; Guo, Z.; Yuan, F.** (2010): Three-dimensional interaction between anchor chain and seabed. *Applied Ocean Research*, vol. 32, no. 4, pp. 404–413.

**Zhao, Y.; Liu, H.** (2013): Large deformation finite element analysis of the anchor line embedded in seabed soils. In *Proceedings of the 32nd International Conference on Ocean, Offshore and Arctic Engineering*, Nantes, France.